# Generative High Resolution Imaging of mmWave Radar from 24GHz to 77GHz

Yeting Song, Hongjun Liu, Sha Tao, Yu Guo, Chao Yao*
School of Computer & Communication Engineering, University of Science and Technology Beijing, Beijing, China

***Abstract*—Millimeter-wave (mmWave) radar at 24 and 77GHz is widely used in autonomous driving, indoor sensing, and security screening. Compared with hardware-friendly 24GHz systems, 77GHz systems provide much higher spatial resolution and richer high-frequency detail sensitive to surface roughness and subtle material differences. Recovering such 77GHz–style structural and material-sensitive detail from 24GHz measurements would enable high-resolution sensing at low cost, but this 24-to-77 cross-frequency generation is fundamentally difficult because much of the high-frequency, material-related information is intrinsically absent at 24GHz and the two bands suffer from geometric misalignment. To address this, cross-frequency generation is reformulated as a generative modeling problem for downstream sensing, and a Joint Spatial–Frequency Generation (JSFG) framework is introduced. JSFG explicitly decouples cross-frequency generation into two complementary objectives in the spatial and frequency domains. In the spatial domain, JSFG regularizes 24GHz observations by suppressing clutter and stabilizing object contours, thereby recovering a clean and reliable low-frequency geometric layout from noisy 24GHz measurements. In the frequency domain, JSFG operates in a multi-scale transform space to refine high-frequency components and to complete the missing frequency-dependent scattering details that characterize 77GHz signals. The experiments show that JSFG substantially outperforms representative mapping and super-resolution baselines in SSIM, PSNR, and amplitude/phase error. Furthermore, in a downstream object-level anomaly detection task using PatchCore, JSFG-generated 77GHz signals yield higher F1 and AUC than using 24GHz inputs or other synthesized 77GHz variants, demonstrating that JSFG improves not only signal fidelity but also downstream sensing performance.**

***Index Terms*—Spatial–Frequency Generation, Mmwave Radar, High Resolution Imaging**

## I. Introduction

In recent years, millimeter-wave (mmWave) radar has been widely deployed in applications such as autonomous driving, smart homes, human–computer interaction, and security screening, owing to its robustness to illumination changes, privacy friendliness, and capability for all-weather sensing [1], [2]. Within this spectrum, Low-frequency 24GHz systems are favored in indoor and consumer scenarios for their low power consumption and strong penetration [3], whereas 77GHz radars offer superior spatial resolution and richer scattering details at the cost of higher attenuation, severe indoor multi-path, increased expense, and stricter radiation constraints [4]. This trade-off naturally motivates cross-frequency generation, aiming to exploit readily available 24GHz measurements to recover 77GHz-level resolution and scattering detail without the cost and deployment burden of full 77GHz hardware.

*Corresponding author. This work was supported by the National Natural Science Foundation of China (62332017and 62303043).

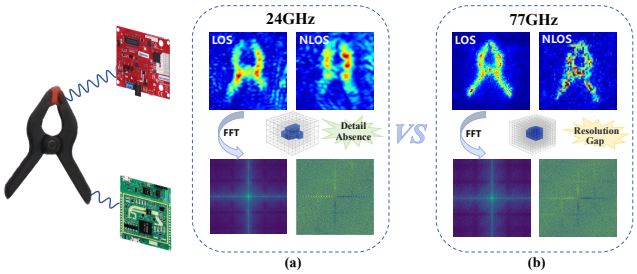


Fig. 1: 24GHz vs 77GHz mmWave Imaging Comparison

In typical millimeter-wave radar imaging systems, received echo signals are usually processed to form range-angle point clouds or radar images [5]. Limited by wavelength differences, the angular and range resolution of 24GHz radar is significantly lower than that of 77GHz, resulting in smoother echoes and limited ability to capture fine contours and micro-motions [6]. However, as shown in Fig.1, we find in the frequency domain that 24GHz and 77GHz radar images have similar low-frequency phase distributions. Since the low-frequency phase primarily encodes the overall geometry and coarse-scale spatial layout of the target, this phenomenon indicates that millimeter-wave imaging at different operating frequency bands exhibits cross-frequency consistency in coarse-scale geometry. In contrast, their high-frequency components differ significantly, the 24GHz response is attenuated and diffused, while the 77GHz response retains the structured high-frequency spectrum associated with sharp edges and fine scattering details.

To bridge the resolution gap between low and high frequency millimeter-wave imaging, recent work has explored learning-based enhancement methods, including frequency-domain interpolation and traditional super-resolution [7]–[9]. However, these approaches mainly operate at the signal level and fail to associate high-frequency components with underlying geometry, leaving the cross-frequency resolution bottleneck unresolved. Millimeter-wave echoes are strongly frequency dependent: at 77GHz, increased sensitivity to surface roughness and geometric details induces complex scattering, whereas such reflections are smoothed or suppressed at 24GHz [10]. Purely data-driven methods neglect these physical priors and tend to generate physically unreliable high-frequency details [11]. Moreover, in complex indoor environments, although 77GHz returns contain rich target information, they

also suffer from strong attenuation, severe noise, and clutter. Consequently, generating 77GHz signals from 24GHz constitutes an ill-posed inference problem that entails information creation and risks amplifying input noise.Consistent with prior super-resolution studies, unconstrained end-to-end models often misinterpret noise as valid features, reducing SNR and introducing structural artifacts.

To cope with the limitations of noisy and low-resolution 24GHz radar imaging, we propose a wavelet-based joint spatial–frequency generation framework. Our goals are two-fold: (1) recovering a clean and physically plausible spatial structure from noisy 24GHz heatmaps, and (2) restoring the missing high-frequency scattering details. Therefore, we extracts multi-scale spatial features in the low-frequency domain to suppress clutter and restore object contours, while enhancing high-frequency components to recover fine details. Specifically, by operating on high-frequency wavelet subbands and learning directional subband–wise residual corrections, the framework reconstructs missing 77GHz scattering details from degraded 24GHz responses. The main contributions of our paper are summarized as follows:

- We formulate 24-to-77 GHz cross-frequency generation as a joint spatial–frequency generation problem and develop JSFG, which treats 24 GHz measurements as a reliable low-frequency structural anchor while inferring only the missing 77 GHz-style material-dependent components under explicit spatial–frequency constraints.
- To address the instability of low-frequency structure, we introduce to model 24 GHz imaging as a frequency-limited blurring of an underlying 77 GHz structural field and exploits this view to design a multi-scale spatial encoder with adaptive, data-driven denoising thresholds.
- To compensate for frequency-dependent scattering differences, we operate directly on 2D-DWT high-frequency subbands. Instead of regressing full wavelet coefficients, the method predicts orientation-aware residual corrections for each directional subband with learnable modulation factors, explicitly modeling the remaining high-frequency responses between synthesized and real 77 GHz signals.

## II. Related Work

We review prior work in two related directions: mmWave radar imaging, which emphasizes frequency-dependent resolution and scattering characteristics, and super-resolution, which aim to reconstruct fine-grained spatial details from sparse or low-resolution measurements.

**Mmwave Radar Imaging:** High-frequency mmWave radars (e.g., 77GHz) deliver fine spatial resolution but remain expensive, power-restricted, and highly sensitive to occlusion noise [1], [2], [4], while low-frequency systems (e.g., 24GHz) offer stronger penetration and lower cost but lack high-frequency scattering details [3], [12]. Existing research has explored cross-frequency imaging and deep-learning reconstruction [13], [14], but traditional multiband fusion often assumes simple frequency superposition or interpolation [8], overlooking frequency-dependent scattering variations. However, a handheld mmWave imaging system yield high-quality contours at short ranges [15], they remain sensitive to occlusion-induced noise. Some approaches enhance 2D/3D radar images via spatial or point-cloud features [16]–[18], but still rely on visible or high-frequency inputs, limiting their applicability to low-frequency mmWave data.

**Super-Resolution:** Neural networks have been widely applied to enhance the resolution of camera and near-infrared images [7], [9]. Inspired by these advances, several studies attempt to extend deep learning–based super-resolution to sparse or low-resolution mmWave radar data [14], [19]. However, unlike optical imagery, low-frequency mmWave signals inherently lack high-frequency structural details due to wavelength-limited spatial resolution and are severely affected by noise, clutter, and multipath artifacts [6], [12]. As a result, purely end-to-end super-resolution models without physical constraints may incorrectly amplify noise as valid structures, leading to spurious artifacts and degraded signal fidelity.

## III. Methods

**Backbone Pipeline:** Given a 24GHz mmWave image $X \in \mathbb{R}^{H\times W\times C}$, we apply a discrete wavelet transform to decompose the input into low and high frequency subbands. The low-frequency component is processed by MSSR through multi-scale convolutions integrated with adaptive denoising to extract spatial structural features, which serve as structural priors for the backbone. Subsequently, the features are fed into a multi-stage encoder–decoder backbone composed of stacked Frequency Enhancement Blocks, operating at different wavelet resolutions and channel dimensions. Within each FEBlock, the Fused Wavelet Convolution Mixer performs global frequency modeling, followed by a feed-forward network for local feature refinement, with MSSR features injected at each stage. Finally, skip connections fuse multi-scale features, and an inverse discrete wavelet transform reconstructs 77GHz image $\hat{Y}$. Fig. 2 shows our architecture.

**Multi-scale Spatial Structure Recovery:** The 24GHz mmWave images exhibit expanded contours and collapsed detail structures due to their wide beamwidth and low angular resolution. This degradation $X$ can be modeled as a spatial convolution with a frequency-limited kernel $\mathcal{K}_{\mathrm{BL}}$

$$X \approx \mathcal{K}_{\mathrm{BL}}(G^*). \tag{1}$$

where $G^*$ denotes the latent structural field associated with 77GHz imaging. To recover sharp and coherent geometry, the input is first processed by a depthwise convolution and a series of multi-scale feature extractors $F_i$, which produce structural embeddings $F_i$. A parallel branch employing global average pooling computes an adaptive denoising threshold $T$ to suppress noise while preserving critical gradients, obtain the feature $\hat{F}_i$.

$$\hat{F}_i = \mathrm{sign}(F_i) \cdot \max\big(|F_i| - \tau_i(p), 0\big). \tag{2}$$

where $\tau_i(p)$ is a spatially varying threshold derived from the global context and local statistics.

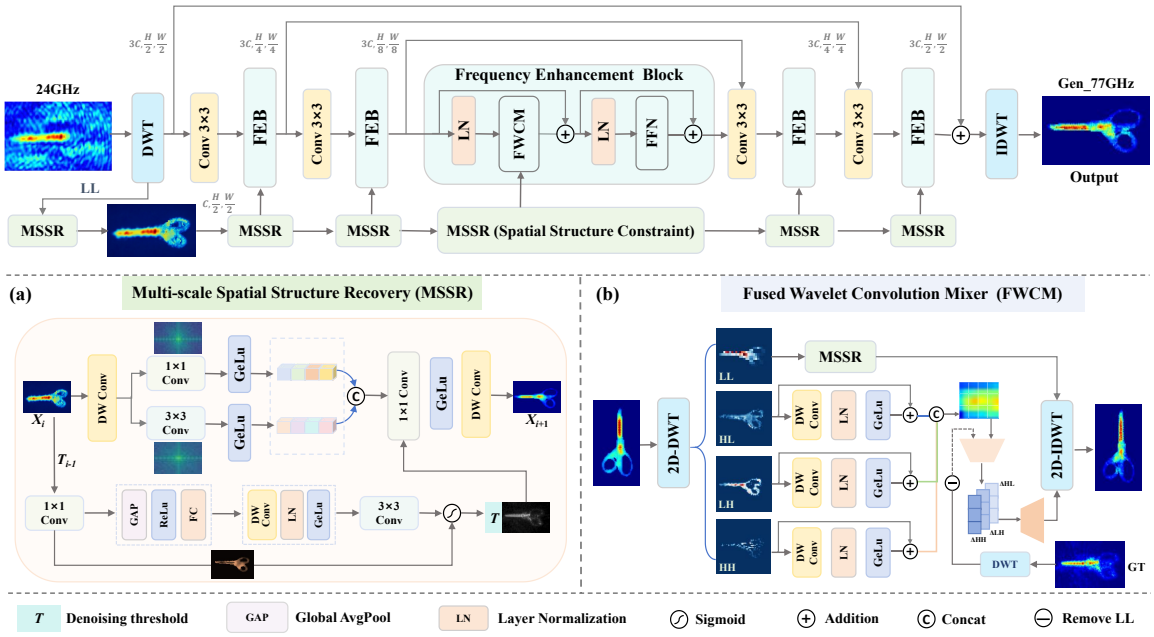


Fig. 2: Overview of Cross-Frequency Signal Generation for high-frequency mmWave Radar Imaging.

Features extracted from different scales are fused via concatenation and subsequently refined through a combination of $1 \times 1$ convolutions followed by nonlinear activation. Finally, well-resolved regions can guide the restoration of weaker areas. The similarity between features at positions $p$ and $q$ is defined as

$$C_{i,j}(p,q) = \exp\left(-\|\psi_i(F_i(p)) - \psi_j(F_j(q))\|^2\right). \quad (3)$$

the $\psi_i$, $\psi_j$ are embedding functions. This process yields a reconstructed field $\hat{G}$ with sharper contours and a coherent multi-scale structure.

**Fused Wavelet Convolution Mixer:** To enhance the high-frequency details while preserving low-frequency structures, we introduce the Fused Wavelet Convolution Mixer (FWCM). Given an input feature map $X \in \mathbb{R}^{H\times W\times C}$, a 2D Discrete Wavelet Transform (2D-DWT) is applied to decompose it into one low-frequency sub-band $W_{LL}$ and three high-frequency sub-bands $\{W_{LH}, W_{HL}, W_{HH}\}$. While $W_{LL}$ mainly captures global layouts and contour structures, $\{W_{LH}, W_{HL}, W_{HH}\}$, corresponding to vertical, horizontal, and diagonal components, are jointly processed by the FWCM to selectively strengthen discriminative edge and texture cues.

$$W_{ij}[k,l] = \sum_m \sum_n X[m,n]\, h_i[2k-m]\, h_j[2l-n]. \quad (4)$$

where $W_{ij}[k,l]$ the output sub-band with $i,j \in \{L,H\}$ indicating low-/high-pass filters along rows and columns $(h_L, h_H)$, $k,l$ the downsampled indices, and $m,n$ denote the row and column indices of the input. Each high-frequency detail component is processed by a dedicated convolutional block with depthwise convolution, LN, and GeLU activation to enhance distinct frequency-specific features.

Given the decomposed wavelet coefficients, the proposed module explicitly predicts residual corrections for each high-frequency subband, with $\Delta R_S \in \Delta HL, \Delta LH, \Delta HH$ corresponding to the horizontal, vertical, and diagonal detail components.Instead of directly regressing full high-frequency coefficients, it learns the missing or degraded scattering responses in each directional subband. The corrected wavelet coefficients are obtained as:

$$\widehat{W}_S = W_S + \gamma_S \cdot \Delta R_S. \quad (5)$$

where $\gamma_S$ is a learnable, scale- and orientation-aware modulation factor that adaptively controls the contribution of each residual correction.

The inverse DWT then reconstructs the spatial-domain output, yielding sparse scattering points, sharp edges, and coherent directional textures, while preserving the low-frequency geometric structure.

**Loss Fuction:** We design a multi-component loss to jointly optimize spatial reconstruction, frequency-domain detail, and cross-domain consistency. Given input $x$ and ground truth $y$, the generator $G(\cdot)$ produces $\hat{y} = G(x)$.The spatial loss enforces pixel-level similarity ($L_1$ term) and preserves structure via $SSIM$.

$$L_{spatial} = |G(x) - y|_1 + (1 - SSIM(G(x), y)) \quad (6)$$

$$L_{frequency} = \sum a,b \left|W_{G(x)}(a,b) - W_y(a,b)\right|^2 \quad (7)$$

Wavelet coefficients $W_{G(x)}(a,b)$ and $W_y(a,b)$ constrain frequency differences to recover high-frequency details.

$$L_{domain} = |F(G(x)) - F(y)|_1 \quad (8)$$

where $F(\cdot)$ denotes a fixed, pretrained encoder for feature extraction. Specifically, features are taken from an intermediate

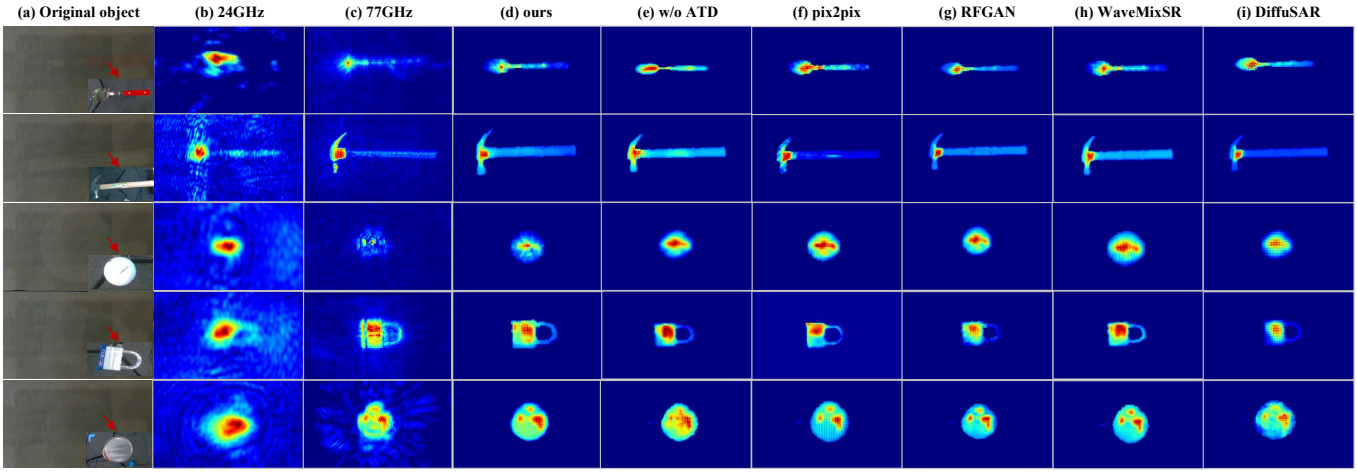


Fig. 3: Cross-frequency generation from 24GHz to 77GHz. Column(a) shows the original objects in line-of-sight (LOS) and non-line-of-sight (NLOS) scenarios.(b) 24GHz radar input. (c) Ground-truth 77GHz radar imaging. (d) Our generated result. (e) Without adaptive threshold denoising. (f–i) Comparisons with pix2pix, RFGAN, DiffuSAR, and WaveMixSR. Our method demonstrates superior boundary preservation and high-frequency scattering recovery.

layer of the generator encoder, whose parameters are frozen during training to capture global structural information without introducing additional learnable constraints.

$$L_{\text{total}} = \lambda_s L_{spatial} + \lambda_f L_{frequency} + \lambda_d L_{domain} \quad (9)$$

$\lambda_s = 0.75$, $\lambda_f = 0.5$, and $\lambda_d = 0.2$ are selected to balance spatial fidelity and frequency enhancement while preventing the feature-domain loss from dominating optimization. A brief sensitivity analysis shows that moderate variations around these values lead to stable performance trends.

## IV. Experiments and Results

### A. Dataset and Implementation Details

**Dataset:** Our work uses the public MITO millimeter-wave radar imaging dataset [12], which provides paired 24GHz and 77GHz mmWave radar measurements captured under both line-of-sight (LOS) and non-line-of-sight (NLOS) conditions. The dataset covers 76 categories of household objects and tools, with synchronized RGB-D images(Fig. 3). Each radar signal, composed of linearly frequency-modulated chirps, is processed via FFT along the sampling, chirp, and antenna dimensions to obtain range, velocity, and angular information, forming a 3D voxel representation $\mathbf{V}_{3D}(\phi, \theta, r)$:

$$\text{Proj}2D(\phi, \theta) = \arg\max r\mathbf{V}_{3D}(\phi, \theta, r) \quad (10)$$

Projecting along the range axis yields a 2D heatmap [16]. Both 24 GHz and 77 GHz data are processed similarly to produce heatmaps $X$ (input) and $Y$ (target), which are resized to $H \times W$ for unified modeling.

**Implementation:** Our experiments are conducted on a Linux platform using PyTorch with CUDA 12.1 on two NVIDIA RTX 4090 GPUs. All experiments data split at the object-instance level to avoid overlap of physical objects or acquisition trajectories between training and testing. The generation framework is trained in two stages. In the first stage, 872 mmWave heatmaps derived from 24 GHz LOS acquisitions are constructed from multiple viewpoints of distinct object instances and further augmented, enabling the model to learn reliable shape correspondence and high-frequency scattering distributions. In the second stage, the model is fine-tuned on 101 NLOS 24 GHz images from disjoint object instances to suppress multipath- and occlusion-induced artifacts. We evaluate JSFG on 320 images, including 98 real NLOS 24 GHz samples, all strictly excluded from the training and validation splits.

### B. Detailed Generation Quality Analysis

**Qualitative Results.** We show JSFG's performance in LOS and NLOS scene, as shown in Fig. 3. In both visbility conditions, JSFG accurately images various targets, preserving the penetration capability of low-frequency radar to mitigate high-frequency noise and capturing object contours and extracting key high-frequency features. Although the GAN model also produces good results, it exhibits frequency distribution biases when generalizing to small objects. As shown in Fig. 4(a), the amplitude histogram of JSFG-generated signals closely matches the real 77GHz (GT), demonstrating the robustness of our generative model. Fig. 4(b) further compares computational efficiency. JSFG achieves better reconstruction quality with fewer parameters and lower FLOPs than competing methods, making it a practical choice for deployment.

**Quantitative Results.** We quantitatively evaluate the generated 77 GHz mmWave data from two perspectives: (i) image-level quality and (ii) complex-domain consistency at the dominant scattering response. Specifically, we report SSIM and PSNR to measure structural similarity and overall reconstruction fidelity in the radar images. In addition, amplitude error and phase error are evaluated only at the dominant scattering response, defined by the argmax-selected range bin for each angular location $(\phi, \theta)$. These metrics quantify the

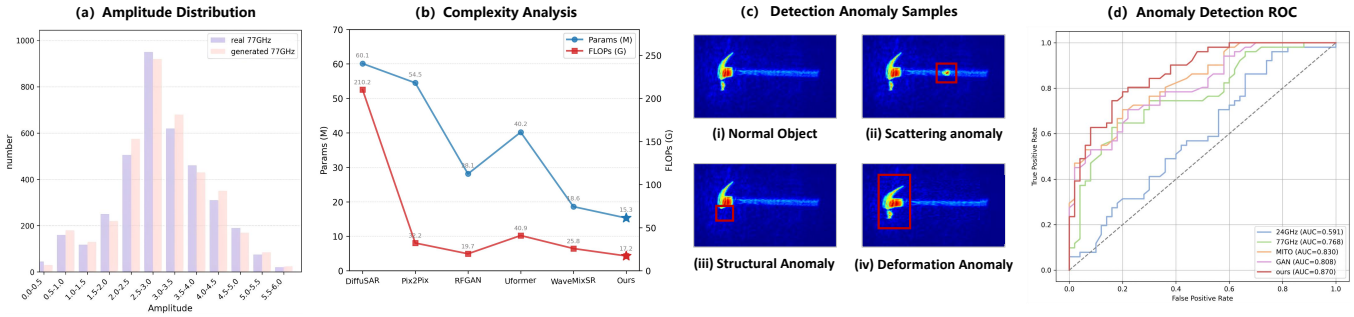


Fig. 4: Evaluation of JSFG-Generated 77 GHz Radar Images and Downstream Anomaly Detection Performance

consistency of the principal scattering component with respect to the ground truth.

TABLE I: Comparison with other methods

| Methods | SSIM | PSNR | Amp_Error | Phase Error |
|---|---|---|---|---|
| DiffuSAR [20] | 0.7558 | 28.47 | 0.3064 | 3.9646° |
| Pix2Pix [9] | 0.7905 | 29.82 | 0.2106 | 4.4260° |
| RFGAN [21] | 0.8259 | 34.95 | 0.1536 | 3.0142° |
| Uformer [22] | 0.8524 | 36.75 | 0.1704 | 3.1124° |
| WaveMixSR [23] | 0.8858 | 37.97 | 0.0935 | 2.1795° |
| ours | **0.9035** | **38.21** | **0.0813** | **1.9527°** |

*Image Quality*: As shown in Table I, our model achieves an average SSIM of 0.90 and PSNR of 38.21 dB across all test samples, indicating strong structural similarity and high reconstruction fidelity in cross-frequency generation. Notably, under occlusion, SSIM remains 0.88, suggesting that the model preserves the overall structure even in challenging scenarios.

*Signal-domain consistency*: As reported in Table I, JSFG achieves an average amplitude error of 0.0813 and a phase error of 1.9527°, indicating improved complex-domain fidelity in cross-frequency generation. Under occlusion, both errors increase slightly, yet the degradation is limited, suggesting robust behavior under challenging conditions. We attribute this improvement to the wavelet-based refinement module, which helps recover high-frequency details around object boundaries and reduces amplitude and phase discrepancies.

*Comparisons*: We compare JSFG with five representative baselines, including generative models such as Pix2Pix [9], RFGAN [21], DiffuSAR [20], and super-resolution approaches include WaveMixSR [23] and Uformer [22]. For a fair comparison, we retrained all models under identical datasets and optimization settings. Table I show that our method consistently outperforms all baselines. In particular, traditional GAN or super-resolution models struggle to model cross-band scattering differences, leading to over-smoothed reconstruction or incoherent phase patterns. By integrating spatial-domain reconstruction with wavelet-domain enhancement, JSFG preserves high-frequency details and achieves superior signal integrity across scenarios.

### C. Ablation Studies

We perform ablation studies to quantify the contribution of each module in the proposed signal generation pipeline.

**Effect of MSSR (denoising).** Removing the proposed denoising module (*w/o MSSR*) causes the average SSIM to drop sharply from 0.90 to 0.78. This degradation is expected because low-frequency representations are particularly vulnerable to background clutter in 24 GHz sensing. In practice, clutter responses can have amplitudes comparable to multipath reflections near object boundaries, which distorts the low-frequency feature distribution and propagates errors to subsequent reconstruction. These results validate the necessity of the adaptive-threshold denoising strategy.

**Effect of FWCM (high-frequency residual refinement).** Disabling FWCM (*w/o FWCM*), i.e., applying the wavelet transform without explicitly modeling the residual between the generated and real 77 GHz high-frequency components, leads to a consistent performance drop. In contrast, incorporating FWCM improves SSIM/PSNR and reduces amplitude error, suggesting that residual refinement helps compensate for material-dependent scattering differences and better recovers boundary-related high-frequency details.

TABLE II: Ablation Study

| Methods | SSIM | | Amplitude Error | |
|---|---|---|---|---|
| | LOS | NLOS | LOS | NLOS |
| Ours | 0.90 | 0.88 | 0.081 | 0.124 |
| w/o MSSR | 0.78 | 0.71 | 0.209 | 0.297 |
| w/o FWCM | 0.86 | 0.83 | 0.120 | 0.158 |
| w/o Fusion model | 0.44 | 0.39 | 0.366 | 0.401 |

**Effect of the fusion model.** We further evaluate the fusion design by removing the integration between the spatial branch and the frequency-domain branch (*w/o Fusion model*). As shown in Table II, this ablation causes a dramatic degradation: SSIM drops from 0.90 to 0.44 in LOS and from 0.88 to 0.39 in NLOS (a relative decrease of about 51% and 56%, respectively). Meanwhile, the amplitude error increases from 0.081/0.124 to 0.366/0.401 (LOS/NLOS), indicating substantially larger complex-domain discrepancies. These results suggest that simply combining heterogeneous spatial and frequency-domain representations (without dedicated alignment/integration) is insufficient, leading to poorly coordinated features and severely compromised reconstruction quality.

### D. Task Evaluation

To evaluate whether JSFG improves downstream perception, we adopt the classical PatchCore architecture [24] for object-

level anomaly detection. Considering the complex-valued, single-channel nature of mmWave radar imaging, the input is reformulated into a three-channel representation consisting of normalized amplitude, structural gradient, and high-frequency residual, and patch-level anomaly scores are aggregated only within object regions to suppress background interference, enabling effective detection of geometric discontinuities, abnormal high-frequency scattering, and object deformation, as illustrated in Fig. 4(c).

TABLE III: Anomaly detection results

| Datasets | Recall | Precision (%) | F1-score | AUC |
|---|---|---|---|---|
| 24GHz | 0.48 | 60.67 | 0.58 | 0.59 |
| 77GHz | 0.78 | 82.51 | 0.81 | 0.77 |
| MITO | 0.82 | 83.09 | 0.82 | 0.83 |
| GAN | 0.85 | 84.92 | 0.84 | 0.81 |
| Ours | 0.85 | 88.03 | 0.87 | 0.87 |

Under identical detection architectures and training protocols, we conduct five independent experiments using 24 GHz, real 77GHz, JSFG-generated 77GHz, MITO-synthesized 77GHz, and GAN-generated 77 GHz as inputs. The model is trained solely on normal samples and evaluated on test sets containing anomalies. As shown in Fig. 4(d), our method achieves an anomaly detection AUC of 0.87, improving upon real 77GHz by approximately 11% and significantly outperforming 24GHz inputs, demonstrating that the generated high-frequency radar images enhance anomaly separability and practical applicability.

## V. Conclusion

In this work, we demonstrate that coupling spatial regularization of 24GHz measurements with frequency-domain residual refinement effectively enables 24-to-77GHz cross-frequency mmWave imaging. The Experiments show that the JSFG framework consistently improves structural similarity, signal-to-noise ratio, and complex-domain accuracy over baselines. The synthesized 77GHz signals support anomaly detection performance comparable to real 77GHz data, even in cluttered or partially occluded scenes. These results indicate that appropriate spatial–frequency generative modeling allows low-frequency sensors to approximate high-frequency capabilities while retaining cost and penetration advantages, offering a practical pathway toward cross-frequency mmWave perception.

## References


[1] Yash Soni, Malhaar Goswami, Nishit Prabhakar Shetty, et al., "Millimeter-wave radar for intelligent sensing: A comprehensive review of techniques, applications, and challenges," *Computers and Electrical Engineering*, vol. 128, pp. 110696, 2025.

[2] A Soumya, C Krishna Mohan, and Linga Reddy Cenkeramaddi, "Recent advances in mmwave-radar-based sensing, its applications, and machine learning techniques: A review," *Sensors*, vol. 23, no. 21, pp. 8901, 2023.

[3] Feraidon Gholami, "Analytical comparison of 24ghz and 60ghz millimetre wave radar sensors," 2025.

[4] Halina Aniołczyk, "Em noise and its impact on human health and safety," *Advanced materials for electromagnetic shielding: fundamentals, properties, and applications*, pp. 11–33, 2018.

[5] Sandeep Rao, "Introduction to mmwave sensing: Fmcw radars, texas instruments," .

[6] Sevgi Z Gurbuz, M Mahbubur Rahman, Emre Kurtoglu, Trevor Macks, and Francesco Fioranelli, "Cross-frequency training with adversarial learning for radar micro-doppler signature classification (rising researcher)," in *Radar Sensor Technology XXIV*. SPIE, 2020, vol. 11408, pp. 58–68.

[7] Wenbin Li, Juefei Li, Jinxin Li, Zhiyong Huang, and Dengwen Zhou, "A lightweight multi-scale channel attention network for image super-resolution," *Neurocomputing*, vol. 456, pp. 327–337, 2021.

[8] Pengfei Xie, Jianxin Wu, Lei Zhang, Guanyong Wang, and Xue Jin, "Resolution enhancement for millimeter-wave radar roi image with bayesian compressive sensing," *Sensors*, vol. 22, no. 15, pp. 5757, 2022.

[9] Phillip Isola, Jun-Yan Zhu, Tinghui Zhou, and Alexei A Efros, "Image-to-image translation with conditional adversarial networks," in *Proceedings of the IEEE conference on computer vision and pattern recognition*, 2017, pp. 1125–1134.

[10] Vasanthan Raghavan, Andrzej Partyka, Lida Akhoondzadeh-Asl, Mohammad Ali Tassoudji, Ozge Hizir Koymen, and John Sanelli, "Millimeter wave channel measurements and implications for phy layer design," *IEEE Transactions on Antennas and Propagation*, vol. 65, no. 12, pp. 6521–6533, 2017.

[11] Bram van Berlo, Amany Elkelany, Tanir Ozcelebi, and Nirvana Meratnia, "Millimeter wave sensing: A review of application pipelines and building blocks," *IEEE Sensors Journal*, vol. 21, no. 9, pp. 10332–10368, 2021.

[12] Laura Dodds, Tara Boroushaki, and Fadel Adib, "Mito: Enabling non-line-of-sight perception using millimeter-waves through real-world datasets and simulation tools," *arXiv e-prints*, pp. arXiv–2502, 2025.

[13] Shahrokh Hamidi, "3d near-field virtual mimo-sar imaging using fmcw radar systems at 77 ghz," in *2024 IEEE Canadian Conference on Electrical and Computer Engineering (CCECE)*. IEEE, 2024, pp. 264–270.

[14] Josiah W Smith and Murat Torlak, "Deep-learning-based multiband signal fusion for 3-d sar superresolution," *IEEE Transactions on Aerospace and Electronic Systems*, vol. 60, no. 1, pp. 8–24, 2023.

[15] Yadong Li, Dongheng Zhang, Ruixu Geng, Zhi Lu, Zhi Wu, Yang Hu, Qibin Sun, and Yan Chen, "A high-resolution handheld millimeter-wave imaging system with phase error estimation and compensation," *Communications Engineering*, vol. 3, no. 1, pp. 4, 2024.

[16] Junfeng Guan, Sohrab Madani, Suraj Jog, Saurabh Gupta, and Haitham Hassanieh, "Through fog high-resolution imaging using millimeter wave radar," in *Proceedings of the IEEE/CVF Conference on Computer Vision and Pattern Recognition*, 2020, pp. 11464–11473.

[17] Martin Dimitrievski, Peter Veelaert, and Wilfried Philips, "Semantically aware multilateral filter for depth upsampling in automotive lidar point clouds," in *2017 IEEE Intelligent Vehicles Symposium (IV)*. IEEE, 2017, pp. 1058–1063.

[18] Yue Sun, Zhuoming Huang, Honggang Zhang, Zhi Cao, and Deqiang Xu, "3drimr: 3d reconstruction and imaging via mmwave radar based on deep learning," in *2021 IEEE International Performance, Computing, and Communications Conference (IPCCC)*. IEEE, 2021, pp. 1–8.

[19] Shaoqiu Song, Yongpeng Dai, Shilong Sun, and Tian Jin, "Efficient image reconstruction methods based on structured sparsity for short-range radar," *IEEE Transactions on Geoscience and Remote Sensing*, vol. 62, pp. 1–15, 2024.

[20] Zilu Ying, Wenyu Ke, Yikui Zhai, Zhihao Long, Jianhong Zhou, Hufei Zhu, and CL Philip Chen, "Diffusar: Frequency domain-aware diffusion model for sar image generation," *IEEE Journal of Selected Topics in Applied Earth Observations and Remote Sensing*, 2025.

[21] M Mahbubur Rahman and Sevgi Z Gurbuz, "Multi-frequency rf sensor data adaptation for motion recognition with multi-modal deep learning," in *2021 IEEE Radar Conference (RadarConf21)*. IEEE, 2021, pp. 1–6.

[22] Zhendong Wang, Xiaodong Cun, Jianmin Bao, Wengang Zhou, Jianzhuang Liu, and Houqiang Li, "Uformer: A general u-shaped transformer for image restoration," in *Proceedings of the IEEE/CVF conference on computer vision and pattern recognition*, 2022, pp. 17683–17693.

[23] Pranav Jeevan, Akella Srinidhi, Pasunuri Prathiba, and Amit Sethi, "Wavemixsr: Resource-efficient neural network for image super-resolution," in *Proceedings of the IEEE/CVF winter conference on applications of computer vision*, 2024, pp. 5884–5892.

[24] Karsten Roth, Latha Pemula, Joaquin Zepeda, Bernhard Schölkopf, Thomas Brox, and Peter Gehler, "Towards total recall in industrial anomaly detection," in *Proceedings of the IEEE/CVF conference on computer vision and pattern recognition*, 2022, pp. 14318–14328.